Journal of Energy Storage 147 (2026) 120193

Contents lists available at ScienceDirect

Journal of Energy Storage

journal homepage: www.elsevier.com/locate/est

Research Papers

Ether-enhanced ionic liquid electrolyte enables robust interphase and fast kinetics for high-voltage $LiNi_{0.5}Mn_{1.5}O_4$

Yuanbo Chen [a,b], Kai Yao [c], Wei Qin [d], Christian Rodenbücher [a], Jiangshui Luo [d], Carsten Korte [a,b,*]

[a] Institute of Energy Technologies–Electrochemical Process Engineering (IET-4), Forschungszentrum Jülich, 52425, Jülich, Germany
[b] RWTH Aachen University, Faculty of Mathematics and Natural Sciences, 52056, Aachen, Germany
[c] Institute of Energy Materials and Devices–Materials Synthesis and Processing (IMD-2), Forschungszentrum Jülich, 52425, Jülich, Germany
[d] College of Materials Science and Engineering, Sichuan University, 610000, Chengdu, China

ARTICLE INFO

Keywords:
Ionic liquid
Anion-rich cationic solvation sheath
5 V cathode
Lithium metal battery

ABSTRACT

The most important key challenge for 5 V-class $LiNi_{0.5}Mn_{1.5}O_4$ (LNMO) lithium metal batteries is to design electrolytes that are stable above 4.5 V while enabling fast Li^+ transport. A promising approach is ionic liquid bases electrolyte, composed of 1-butyl-1-methylpyrrolidinium bis(fluorosulfonyl)imide ($Pyr_{14}FSI$) and lithium bis(fluorosul-fonyl)imide (LiFSI), where both the Li^+ concentration and the amount of a fluoroether-based co-solvent (BTFE, bis(trifluoroethyl)ether) are independently adjusted to achieve a multidimensional control over the local Li^+ solvation environment. The Li^+ solvation sheath can be reshaped to a compact, anion-rich configuration, characterized by full-contact ion pairs (FCIPs) and enhanced Li^+–FSI^- coordination by adjusting the LiFSI and BTFE ratio. The ionic conductivity is markedly enhanced from 0.49 to 1.34 mS cm^{-1}, and the anodic stability window is extended up to 5.4 V *vs.* Li/Li^+. Most crucially, a rapid formation of a dense, oxidation-resistant cathode–electrolyte interphase (CEI) during the initial charge cycle can be observed for systems with anion-rich solvation sheath, thereby suppressing further electrolyte oxidation and mitigating impedance growth. As the results, LNMO cells employing the optimized electrolytes retain 84.1 % of their initial capacity after 100 cycles, compared to only 30.68 % after 70 cycles for carbonate based electrolytes. This work provides a reference for the effect of ether co-solvents on the coordination structure of Li^+ in ionic liquid electrolytes and explores the use of such electrolyte in 5 V high-voltage lithium secondary battery systems with LNMO as the cathode.

1. Introduction

High energy density in lithium-based rechargeable batteries has become a key requirement to meet the stringent performance demands of next-generation energy storage applications [1,2]. Combining a high specific capacity (3860 mAh g^{-1}) and low electrochemical potential (−3.04 V *vs.* standard hydrogen electrode) lithium metal anode with specific high-voltage cathodes offers an effective means to enhance the overall energy density of battery systems [3–5]. Among various candidates, the spinel-type oxide LNMO emerges as a promising cathode material for next-generation high-voltage battery systems, owing to its attributes of high operating voltage (~5.0 V, *vs.* Li^+/Li), substantial specific capacity (147 mAh g^{-1}), cost-effectiveness (Co-free), elevated conductivity, and structural stability [6,7]. Despite these advantages, alkylcarbonate-based electrolytes used in state-of-the-art commercial lithium cells possess a limited electrochemical window (0.5–4.5 V *vs.* Li^+/Li). Their poor reduction stability leads to reactive interfaces on graphite and unstable SEI layers on lithium metal, while their limited oxidation stability (>4.1 V) leads to severe cathode-electrolyte side reactions, causing rapid degradation and safety concerns [8,9]. Strategies such as self-supported configurations [10,11], surface coatings [12], or internal doping [13], provide partial improvements but do not fundamentally suppress parasitic reactions. On the electrolyte side, increasing lithium-salt concentration suppresses oxidative dehydrogenation by reducing free-solvent content and driving a transition from solvent-separated ion pairs (SSIP) to contact-ion-pair (CIP) structures [14,15]. Anion-rich CIP solvation sheath generates protective layers under oxidative conditions, thereby stabilizing the cathode interphase, modifying the EDL, and extending the electrochemical window [16,17]. However, solubility limits impose an upper bound on "solvent

---

* Corresponding author at: Institute of Energy Technologies-Electrochemical Process Engineering (IET-4), Forschungszentrum Jülich, 52425, Jülich, Germany.
E-mail address: c.korte@fz-juelich.de (C. Korte).

https://doi.org/10.1016/j.est.2025.120193
Received 7 October 2025; Received in revised form 29 November 2025; Accepted 26 December 2025

depletion" strategies [18].

Ionic liquids (ILs) provide an alternative pathway due to their inherent thermal stability, wide electrochemical window, negligible vapor pressure and exceptional tunability through the selection of various cation-anion combinations and functional groups [19–21]. They consist entirely of bulky organic cationic and anionic species, resulting in a low lattice energy and thus a low melting temperature, *i.e.* ILs are salts molten at room temperature. Among the various IL families, those containing fluorinated anions and saturated alkyl cations exhibit excellent stability toward both metallic alkali metals and high-voltage cathode materials [22,23]. Specifically, electrolytes based on the fluorosulfonylimide (FSI^-) anion combined with pyrrolidinium cations have attracted significant attention. The presence of FSI^- anions, owing to their smaller and more compact structure compared with $TFSI^-$, weakens cation–anion interactions and results in markedly lower viscosities in the corresponding ionic liquids (*e.g.* 53.2 mPa·s for $Pyr_{14}FSI$ compared with 77.8 mPa·s for $Pyr_{14}TFSI$ at 298 K) [24]. In addition, FSI^- based electrolytes have been reported to undergo interfacial reactions with fewer parasitic pathways and substantially lower gas evolution than alkyl-carbonate systems at high voltages (>4.5 V) [25–28], and their reduction products are often associated with the formation of compact, inorganic-rich interphases that help stabilize the electrode–electrolyte interphase [28,29]. Futhermore, PDOS and cluster-level electronic structure analyses indicate that the lowest-energy acceptor states of the Li^+ solvation complex are predominantly localized on FSI^- derived orbitals, ensuring a continuous supply of precursors for solid electrolyte interphase formation [30,31]. Despite these attributes, the viscosity of ionic liquids remains substantially higher than that of molecular solvents, which poses a kinetic limitation. Consequently, many studies adopt relatively dilute IL electrolytes, as illustrated by Yang et al. [32] using 1 M LiTFSI and Tu et al. [33] using 1.5 M LiFSI in pyrrolidinium-based ionic liquid, both demonstrating stable cycling for $LiFePO_4$ cathodes. Nevertheless, most studies on ionic liquids as electrolytes for lithium-ion batteries focus on dilute lithium salt concentrations below 1.5 M, with limited reports on their practical application in high-voltage cathodes. To overcome the trade-off between the high viscosity of ionic liquids and their superior electrochemical stability, the incorporation of low-viscosity non-solvating diluents has emerged as an effective mitigation strategy. All-fluorinated alkylether like bis-(2,2,2-trifluoroethyl) ether (BTFE) as solvents, characterized by a low viscosity, have been identified as ideal diluents for high-concentration electrolytes in lithium metal batteries (LMBs). BTFE diluent molecules, surrounding the clusters of Li^+ with anions in the solvation sheath, could co-participate to the electrolyte/electrode interphase formation, enhancing the interphase properties and improving the electrolyte conductivity. The efficacy of this "non-solvating dilution" strategy has been widely demonstrated in conventional organic solvent systems. For instance, Yu et al. [34] and Chen et al. [35] utilized BTFE to modify LiFSI-based carbonate and ether electrolytes (1.2 M), respectively, which significantly improved the cycling stability of NMC111 cathodes by decoupling ionic transport from interfacial chemistry. Furthermore, Ono et al. extended this concept to ultra-high concentration systems, combining ~4 M $LiNO_3$ with NMP and BTFE to enable stable operation of lithium-oxygen batteries [36]. These studies raise the question of whether this diluent can be applied in highly concentrated IL-based electrolytes to mitigate low electrolyte conductivity, sluggish electrode kinetics and to obtain Li^+ solvation structures that provide robust cathodic interphase protection. This inquiry motivates us to explore the design of novel electrolyte with ether-based co-solvent and anion-rich high-concentration IL. Additionally, a comprehensive understanding of Li^+ solvation structures that enhance interfacial stability and Li^+ transport kinetics at the high-voltage cathode (5 V) interphase is imperative.

Herein, this study presents an investigation of the interactions of the various components in ionic liquid-based Li^+ electrolytes, allowing cationic solvation sheath with an increased number of anionic species, forming a $[Li\ (anion_x)]^{x\text{-}1}$ complex (so-called electrolytes with an "anion-rich" solvation sheath) and the consequences for the application in high-voltage (5 V) lithium metal batteries. We selected the IL $Pyr_{14}FSI$, the lithium salt LiFSI and the co-solvent BTFE to obtain an electrolyte with a full-contact ion pair (FCIP) solvation structure, in which Li^+ is densely coordinated by FSI^- anions without free solvent molecules. This compact, anion-rich configuration arises from the eutectic nature of the mixture and facilitates a more saturated local environment than the aggregated ion environments generally observed in concentrated electrolytes. BTFE is introduced as a non-solvating diluent to mitigate the low conductivity and sluggish kinetics inherent to the pure ILs. The optimized electrolyte provides an electrochemical stability window up to 5.4 V and forms a compact inorganic CEI that improves interfacial kinetics and supports stable high-voltage operation. These results offer a practical direction for developing ionic liquid based electrolytes for 5 V lithium metal batteries.

2. Experimental section

2.1. Materials preparation

All employed chemicals were dried at appropriate temperatures before use. Lithium bis-(fluorosulfonyl)imide (LiFSI, Solvionic, 99.9 %) and 1-Butyl-1-methylpyrrolidinium bis-(fluorosulfonyl)imide ($Pyr_{14}FSI$, Solvionic, 99.9 %) were dried at 110 °C and 60 °C in vacuum (<0.1 ppm) for 24 h, respectively. Bis-(2,2,2-trifluoroethyl)ether (BTFE, Sigma-Aldrich, 98 %) was dried over activated molecular sieves (Alfa Aesar, 0.3 nm) for one week. As a reference electrolyte, the commercially available LP30 (1 M $LiPF_6$ in EC/DMC, 1:1 v/v; Solvionic) was employed throughout the study. Lithium metal foil (thickness 0.5 mm, 99.9 %, AOTELEC) and $LiNi_{0.5}Mn_{1.5}O_4$ (MTI Corp, USA) were used as received. Glass fiber separators (Whatman GF/D) were dried at 120 °C under vacuum (<1 mbar) for 48 h.

The electrolyte preparation was conducted in an argon-filled glove box with levels of water (H_2O) and oxygen (O_2) maintained below 0.1 parts per million (ppm). For the $Pyr_{14}FSI$/LiFSI/BTFE ternary electrolyte, the mixture of $Pyr_{14}FSI$ and LiFSI was subjected to stirring overnight at 60 °C, after which BTFE is added and the stirring is continued for an additional 48 h. The lithium salt concentration in $Pyr_{14}FSI$ ionic liquid was varied from 1 mol/L (PLF-1M) to 3 mol/L (PLF-3M). In the high-concentration ionic liquid electrolyte (PLF-3M), the molar ratio of Pyr_{14} cation to BTFE molecule was adjusted from 10:3 (PLF-3M-0.3B) to 1:1 (PLF-3M-1.0B).

The $LiNi_{0.5}Mn_{1.5}O_4$ (LNMO) cathodes were fabricated by using doctor-blade casting on aluminum foil of slurries based on 1-Methyl-2-pyrrolidone (NMP), comprising 90 wt% of the active material (LNMO), 5 wt% super carbon black (CB, Timcal Super C65) and 5 wt% PVdF (Polyvinylidendifluoride) binder (PVdF, Targray D-2). The slurry was prepared by milling for 60 min in a ball mill. Following the evaporation of the solvent NMP in an oven at 80 °C, electrodes with a diameter of 14 mm were punched out and subsequently dried under vacuum (< 1 mbar) at 100 °C for 12 h. After weighing in a desiccated environment, the electrodes were dried at 110 °C under vacuum (<1 mbar) for an additional 4 h before being transferred to the Ar-filled glovebox.

2.2. Materials characterization

An FTIR spectrometer (Thermo Scientific, USA) equipped with an ATR unit (Monolithic Diamond GladiATR, PIKE Technologies, USA) was utilized to record the IR spectra. Raman measurements were conducted at an excitation wavelength λ of 785 nm (laser from Oxxius). The scattered light was gathered by a large-aperture microscope objective and directed to a spectrograph (Andor Shamrock SR-303i-A; Czerny–Turner configuration, 800 lines/mm diffraction grating, 80 μm slit) *via* a dichroic mirror and a plano-convex lens. The thermal behavior of the electrolytes was investigated through thermogravimetry (TGA, PerkinElmer STA 6000). The crystal structure of the as-prepared cathode samples and the absence of other crystalline phases were determined by powder X-ray diffraction (XRD, Bruker D8 ADVANCE A25X, Cu-K$_\alpha$: $\lambda = 1.5418$ Å) at a scan rate of 2° min^{-1} in the 2θ range of 5–90°. The chemical valence state of elements for the samples were analyzed by X-ray photoelectron spectroscopy (XPS) using a ThermoFisher EscaLab Xi$^+$system equipped with a monochromatic Al-K$_\alpha$ source. The electrochemical studies were performed using a Solartron Analytical 1400 Cell Test System (Ametek, USA). Transmission electron microscopy (TEM and HRTEM) investigations and selected area electron diffraction (SAED) were performed by employing a Talos F200S Super-X (acceleration voltage of 200 kV). The active material was subjected to two activation cycles and one subsequent initial cycle in a coin cell before being characterized by XPS and TEM. The morphology, size, and microstructure were characterized by scanning electron microscopy (SEM, Zeiss Gemini Ultra Plus and Oxford Ultim Max 100 with a field emission electron gun).

2.3. *Electrochemical measurements*

For the electrochemical measurements, coin cell bodies (CR2032) and EL-cells (EL-Cell, Germany) were used. All Li||LNMO, stainless steel||stainless steel, Li||Cu coin cells and EL-Cells were assembled in an argon-filled glovebox (<0.1 ppm of O_2 and H_2O). An amount of 120 μL electrolyte was added before sealing the EL-cells and crimping the coin cells.

Galvanostatic charge/discharge (GCD) cycling of the Li||LNMO EL-cells was performed at 0.1C within a cutoff voltage window between 3.5 V and 5.0 V on a Solartron Analytical 1470E/1451A multi-channel CellTest system. The total conductivity was investigated by using stainless steel||stainless steel test cells. The bulk resistance obtained at 1 kHz was used to calculate the ionic conductivity. The Li plating/stripping Coulombic efficiency (CE) was measured in Li||Cu cells at a current density of 0.5 mA cm^{-2} and an areal capacity of 1 mAh cm^{-2} using a CT 3008 cycler (NEWARE). Linear sweep voltammetry (LSV) curves were obtained for Li||Al cells in the range from open-circuit voltage to 7.0 V at 10 mV/s using a Solartron Analytical 1470E/1451A multi-channel CellTest system. Electrochemical impedance spectroscopy (EIS) was conducted over a frequency range from 100 kHz to 0.01 Hz and an alternating voltage amplitude of 5 mV. The diffusion coefficient (D_{Li}) can be derived from the expression as:

$$\widetilde{D}_{\mathrm{Li}} = \frac{1}{2}\left[\left(\frac{V_{\mathrm{m}}}{F\,A\,\sigma}\right)\left(\frac{dE}{dz}\right)\right]^2 \tag{1}$$

where V_{m} is the molar volume of LNMO cathode, F is the Faraday constant, A is the total contact area between the electrode and the electrolyte, dE/dZ is the slope of charge/discharge curves, and σ is the Warburg coefficient. It is determined as the fitted slope of Z' *vs.* $\omega^{1/2}$ plot, where ω is the angular frequency. The experimental data were fitted by Z-View software (version 2, Scribner Associates Inc.) using an equivalent circuit as a model. The DRT was calculated using the open-source DRTtools software, with consistent parameter settings across different EIS tests to ensure reliable results. All electrochemical tests were conducted at 25 °C.

2.4. *Theoretical calculations*

All molecular dynamics (MD) simulations were conducted based on Forcite package in Materials Studio (Version 8.0) to model Li$^+$ coordination environments in different electrolyte compositions. The PLF-1M and PLF-3M ionic liquid electrolyte solutions were simulated using 505 Pyr$_{14}$FSI and 125 LiFSI molecules, and 169 Pyr$_{14}$FSI and 125 LiFSI molecules, respectively. In addition, the PLF-3M-0.3B and PLF-3M-1.0B ionic liquid electrolyte system included 51 and 169 BTFE molecules, respectively. The COPASS III force field was applied. The simulation were initially equilibrated under NVE conditions (constant volume and total energy) for 200 ps. Subsequently, the production simulations were executed under NPH conditions (constant pressure and enthalpy) for another 1000 ps. Finally, simulation were carried out under NVT conditions (constant volume and temperature) for another 2000 ps to ensure structural and thermodynamic stabilization. The temperature was controlled using a Nosé thermostat with a target temperature of 298 K. DFT calculations were conducted using the DMol^3 module in Materials Studio software. The geometry optimizations and LUMO/HOMO energy calculations were performed employing the Generalized-Gradient Approximation (GGA)/Perdew-Burke-Ernzerhof (PBE) functional [37] and a Double Numeric Polarization (DNP) basis set.

3. Results and discussion

3.1. *The bulk structure and properties of the ionic liquid electrolyte*

3.1.1. *TGA measurements and bulk electrochemical properties*

Fig. 1(a) illustrates the concept of anionic full-contact-ion-pairs IL electrolytes designed to optimizing the anion-to-Li$^+$ ratio in the solvation sheath of Li$^+$ while controlling organic cation transport. The introduction of additional anions and Li$^+$ reduces the spacing between individual Li$^+$ solvation sheath, leading to a more densely packed ionic environment and promoting the formation of supersaturated organic cation-anion complexes. On this basis, a trace amount of low donor number (DN) ether solvent BTFE can promote more free anions to enter the Li$^+$ solvation sheath, enabling maximum coordination to form the anionic full-contact-ion-pairs, while maintaining strong organic cations-anions interactions. Within the ternary system, Pyr$_{14}$FSI and LiFSI form a composition range with a small miscibility gap, whereas BTFE is miscible with Pyr$_{14}$FSI but does not solvate LiFSI. Although LiFSI is essentially insoluble in pure BTFE, the ionic liquid matrix enables all three components to form a macroscopically homogeneous phase. Consequently, the overall system remains macroscopically homogeneous throughout the investigated composition range. Although minor microscopic variations may exist in multicomponent ionic systems, all electrolyte systems in this study remained visually homogeneous for several months. This approach offers valuable insights into tuning the solvation structure in IL electrolytes to enhance its applicability in high voltage (>4.5 V) LMBs.

The electrolyte samples with different component ratios regarding ionic liquid, conductive salt and co-solvent were investigated by TGA measurements as presented in Fig. 1(b). The co-solvent BTFE in PLF-3M-0.3B and PLF-3M-1.0B completely evaporates below 100 °C. The ratio of co-solvent to Pyr$_{14}^+$ cations is about 3:10 and 1:1, respectively, which corresponds to the observed step. At approximately 300 °C, a strong mass loss indicates the initial decomposition of the FSI$^-$ anions [38]. This corresponds to the characteristic decomposition temperature of the FSI$^-$, as reflected in the DTA diagram in Fig. 1(c). The thermal analysis indicates that this electrolyte system can remain stable within the normal operating temperature range of lithium metal batteries.

The electrochemical stability of different electrolyte systems have been evaluated using LSV. Fig. 1(d) shows that the oxidation onset for the reference LP30 electrolyte appears at 3.3 V (*vs.* Li|Li$^+$). A second process emerges near 4.1 V (*vs.* Li|Li$^+$), corresponding to further EC/DMC oxidation and the formation of an AlF_3 passivation layer on the aluminum surface [39]. In contrast, the oxidation current begins to increase above 4.5 V (*vs.* Li|Li$^+$) in the ionic liquid electrolytes with 1 M lithium salt concentration. Compared to LiPF$_6$-based systems, LiFSI-based formulations also exhibit lower acid-driven degradation, contributing to higher oxidative stability [39,40]. After that, the oxidation current begins to increase apparently above 5.1 V (*vs.* Li/Li$^+$), indicating that more densely packed ionic environment and the formation of supersaturated organic cation-anion complexes effectively broadens the electrochemical stability window. The electrochemical

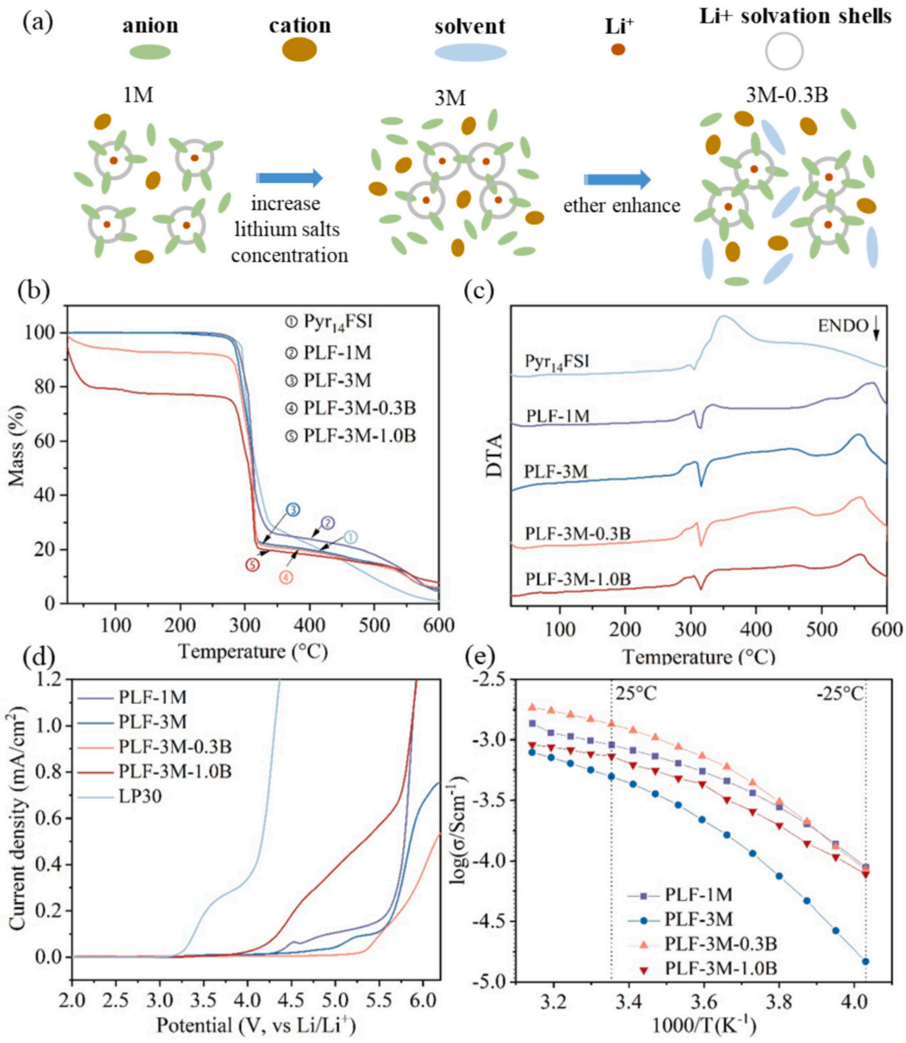

Fig. 1. Thermodynamic and electrochemical properties of $Pyr_{14}FSI$-based ionic liquid electrolytes. (a) Schematic illustration of the concept of anionic full-contact-ion-pairs (FCIPs) and the role of BTFE in promoting anion-rich Li^+ solvaton sheath. Additional anions and Li^+ can modify the coordination structures and restrict the transport of organic cations. Based on this, trace ether diluents further adjust the local coordination environment, increasing the anion content in the Li^+ solvation sheath and promoting the formation of anionic full-contact-ion-pairs; (b) TG and (c) DTA curves of different electrolytes in air; (d) Linear sweep voltammetry (LSV) curves of Li||Al cells. Scan rate: 10 mV/s; (e) log σ *vs.* 1000/*T* plots of the SS||SS cells measured from −25 and 45 °C.

stable window reached its maximum of 5.4 V after anionic full-contact-ion-pairs were formed. However, excessive addition of co-solvents disrupts the compact ionic environment, leading to premature oxidative decomposition at 4.2 V. As shown in Fig. 1(e), compared with PLF-3M ILEs, the total conductivity of PLF-3M-0.3B ILEs increases from 0.49 to 1.34 mS cm^{-1}. This enhancement lowers interfacial polarization and promotes more uniform interfacial reactions during high-voltage cycling. Additionally, the contact angle decreases from 82.8° to 63.8° (Fig. S1), indicating enhanced wettability. It also exhibits high ionic reversibility, maintaining a Coulombic efficiency of 98 % after 3 cycles in Li||Cu cells (Fig. S2).

3.1.2. Solvation structure analysis

In Fig. 2(a-c), the FTIR spectra of the $Pyr_{14}FSI$-based ionic liquid electrolytes with different ratios of the co-solvent BTFE are depicted. An assignment of the vibration modes of pure $Pyr_{14}FSI$, PLF-3M, and PLF-3M-0.3B are provided in Table S1. After adding the co-solvent BTFE, peaks located at around 677, 950, and between 1250 and 1325 cm^{-1} appear. They can be tentatively attributed to asymmetric ν_{as} and symmetric stretching modes ν_s of the C–O–C and C–F bonds of BTFE [41,42]. According to the literature, the continuous broadening of the peaks at 592.1, 731.4, 827.3, and 1102.6 cm^{-1}, along with that of the peaks at higher wavenumbers in the range of 2870–2970 cm^{-1}, depicted in Figs. 2(a-c) and S3, suggests the presence of higher levels of ion pairing such as doubles, triples, and polymer-like aggregates [43–45]. A shoulder peak appears at around 592.1 cm^{-1}, see Fig. 2(b), is increasing in intensity with increasing salt concentration. This may also be caused by a coordination interaction between the added Li^+ ions and FSI^- anion. As the concentration of the lithium salts is increasing, the peaks at 731.4 and 827.3 cm^{-1} in Fig. 2(c), assigned to ν_s(SNS), ν_{as}(SNS), and ν(SF) modes, show noticeable shifts to higher wavenumbers. According to Beran et al., this implies that Li^+ undergoes coordinative interactions with the FSI^- anions, leading to conformation changes of the FSI^- anions and causing a shift of the corresponding modes to higher frequencies [46]. At the same time, the peak at 565 cm^{-1}, which can be assigned to $\delta_a(SO_2)$ mode, exhibits a slight shift also toward higher wavenumbers with increasing concentrations of the lithium salt and the co-solvent. This indicates an enhancement in the coordination between the FSI^- and Li^+.

The interactions among the ionic species and the neutral solvent BTFE were also analyzed through Raman Spectroscopy, see Figs. 2(d, e) and S4. According to the literature, the peaks at around 292 and 355 cm^{-1} correspond to the anti-conformer of FSI^-, while the peaks at around 298 and 352 cm^{-1} are associated with the syn-conformer [47].

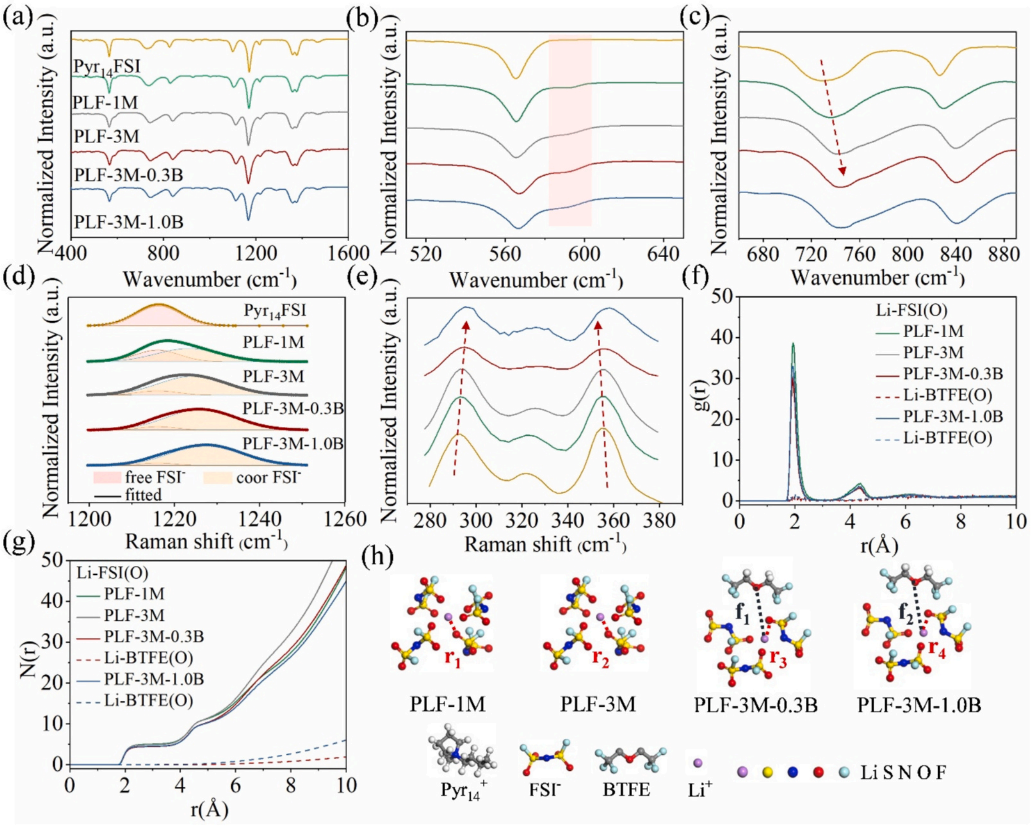

Fig. 2. Spectroscopic characterization and molecular dynamics analysis of Li^+ solvation structures in $Pyr_{14}FSI$-based electrolytes. (a-c) FTIR spectra in the ranges 400–1600, 490–650, and 650–900 cm^{-1}; (d, e) Raman spectra in the1200–1250 cm^{-1} and 280–380 cm^{-1}; (f) radial distribution functions (RDFs) and (g) integrated RDFs obtained from classical molecular dynamics simulation for PLF-1M, PLF-3M, PLF-3M-0.3B, and PLF-3M-1.0B electrolytes; (h) molecular structure of the present (ionic) species in the electrolytes.

As depicted in Fig. 2(e), upon the addition of lithium salt and co-solvent, the peak at 292 cm^{-1} shifts to a higher wavenumber, while the peak at 355 cm^{-1} shifts slightly to a lower wavenumber. Additionally, both peaks exhibit gradual broadening. This implies that in neat $Pyr_{14}FSI$—before adding the lithium salt and the co-solvent—the anti-conformer of $FSI^-$is dominating. The syn-conformer became the majority species when the lithium salt and co-solvent were dissolved in neat $Pyr_{14}FSI$. The peak at 1210–1250 cm^{-1} corresponds to a vibration mode of the SO_2 functional group of the FSI^- anion [48]. When increasing the lithium salt and co-solvent content, the maximum shifts to lower wavenumbers and an asymmetry can be observed, see Fig. 2(d). It can be deconvoluted into two components (gaussian functions). The first component (pink area) at 1216 cm^{-1} corresponds to free FSI^- anions, while the second component (yellow area) at 1225 cm^{-1} represents FSI^- anions coordinated to Li^+.

As the salt concentration and co-solvent ratio increase, the proportion of free FSI^- anions continuously decreases. The fraction f of Li^+-coordinated FSI^- is given as:

$$f = \frac{s_2}{s_1 + s_2}$$

Hereby, s_1 and s_2 are the peak areas obtained from deconvolution. The average number n of FSI^- coordinating to each Li^+ yields as:

$$n = \frac{f}{x}$$

x represents the molar fraction of Li^+ relative to the total cations in system. Through peak fitting and quantitative analysis, we found that the addition of the co-solvent promotes the coordination between the anion and Li^+, see Table 1, forming a more closely packed solvation sheath around the Li^+.

Table 1
The fraction f of Li^+-coordinated FSI^- and average number n of FSI^- anions coordinated to each Li^+ ion for the investigated ionic liquid-based electrolytes.

Sample	f	n
$Pyr_{14}FSI$	0	0
PLF-1M	0.63	3.16
PLF-3M	0.88	2.06
PLF-3M-0.3B	0.91	2.15
PLF-3M-1.0B	0.94	2.21

For a deeper understanding of the solvation structure of Li^+ in the electrolyte, we conducted molecular dynamics simulations to model the coordination of Li^+ in different electrolyte compositions, see Figs. 2(f-h) and S5. The radial distribution functions (RDF) $g(r)$ were computed to provide a more in-depth characterization of the coordination relationship between Li^+ and other components in the electrolyte. The RDF curves reveal a continuous decrease of the g(r) values with increasing lithium salt concentration. Accordingly, the calculated coordination number between FSI^- and Li^+ decreases from 5.04 to 4.49. The distance between Li^+ and the oxygen atom of FSI^-(O) is denoted as r_i, while the distance between Li^+ and the oxygen atom of BTFE(O) is defined as f_i for each system. After addition of the co-solvent, the coordination number of Li^+ slightly increases to 4.55, and the radial size of the first solvation sheath is slightly larger ($r_3 > r_4 \approx r_2 \approx r_1$; $f_1 > f_2$), see Fig. 2(h). Subsequently, when increasing the proportion of co-solvent in high-concentration electrolytes leads to a re-increase of the coordination number of Li^+ regarding FSI^-. This is consistent with the conclusions based on the IR and Raman spectra, which indicate a change in the local coordination environment of the FSI^- anions. At the same time, we also observe that the co-solvent BTFE does not participate in the first solvation sheath of Li^+; instead, it is distributed around the periphery of the first solvation sheath.

3.2. *The LNMO electrode and Li storage behavior*

3.2.1. *XRD and SEM investigations*

The cathode material $LiNi_{0.5}Mn_{1.5}O_4$ (LNMO) can exist in two phases with different crystal structures, depending on the preparation, respectively, on the thermal treatment. There is a spinel-type phase (AB_2O_4) with a Fd3¯m space group, *i.e.* O-ions on 32e sites, Li-ions on 8a sites (A) and a random (disordered) occupation of Ni and Mn ions on the 16d sites (B). An ordered occupation of this site results in a second phase with a cubic structure and the $P4_332$ space group, thus with a lower symmetry. For an application as cathode material in a secondary battery the (disordered) spinel phase has more benign properties regarding cycling behavior.

The purity of the purchased spinel-type LNMO was determined through XRD Rietveld refinements, as illustrated in Fig. 3(a). The assumed atomic positions in nonstoichiometric $LiNi_{0.5}Mn_{1.5}O_4$ were as follows: Li atoms occupied the 8a sites, while Ni and Mn atoms were situated on the 16d sites, and the O atoms were positioned on the 32e sites. The presence of other impurity phases in the LNMO samples is minimal, as no small peaks related to NiO, MnO were observed at positions 15.3°, 39.7°, 45.7°, 57.5° and 65.6° [49]. As expected, all peaks of the $LiNi_{0.5}Mn_{1.5}O_4$ XRD profiles can be excellently fitted, exhibiting a remarkable conformity to the $Fd\bar{3}m$ space group. However, a possible ordering of the Ni and Mn ions, implied by the presence of the second cubic phase with the space group $P4_332$ cannot be distinguished simply by XRD, as the scattering factors of Ni and Mn are much too similar. The structural parameters derived from the fitting process were presented in Fig. 3(a), accompanied by a w_R value of 10.007 [50]. The fitted lattice parameter of 8.170 Å is slightly larger than the reported value for stoichiometric LNMO (8.166 Å), which can be attributed to the presence of a small amount of Mn^{3+} ions, consistent with slight deviation from ideal stoichiometry [51].

The morphology of LNMO particles was determined through SEM investigations. As shown in Fig. 3(b, c), the LNMO samples exhibits particle sizes ranging from 3 to 6 μm. The elemental distribution in the LNMO particles was further characterized using EDS. As depicted in Fig. 3(d–f), Ni, Mn, and O elements were uniformly distributed across the particles.

3.2.2. *Electrochemical investigation*

The 1st cycle of a galvanostatic charge-discharge measurement in a potential range between 3.5 and 4.9 V of a cell with an LNMO cathode, Li anode and the ionic liquid-based electrolyte PLF-3M-0.3B (with “anion-rich” Li^+ solvation sheath) is depicted in Fig. 4(a) and (b). The charging curve consists of two platform regions with nearly constant voltage and three inclined regions. This illustrates the existence of two broad two-phase regions and three narrow solid-solution regions. Specifically, the two-phase regions indicate that the LNMO electrode is undergoing a minor oxidation-reduction process at approximately 4.2 V and a primary charge/discharge oxidation-reduction process at around 4.7 V. The former can be associated with the oxidation-reduction of Mn ions, *i.e.* Mn^{3+}/Mn^{4+}, while the latter was related to the redox reaction of Ni^{2+}/Ni^{3+} and Ni^{3+}/Ni^{4+}, which were as follows:

$$Li_{1+x}Ni^{II}_{0.5}\left(Mn^{III}_{x}Mn^{IV}_{1-x}\right)_{1.5}O_4 \rightleftharpoons LiNi^{II}_{0.5}Mn^{IV}_{1.5}O_4 + x\,Li^+ + x\,e^-$$

$$LiNi^{II}_{0.5}Mn^{IV}_{1.5}O_4 \rightleftharpoons Li_{0.5}Ni^{III}_{0.5}Mn^{IV}_{1.5}O_4 + 0.5\,Li^+ + 0.5\,e^-$$

$$Li_{0.5}Ni^{III}_{0.5}Mn^{IV}_{1.5}O_4 \rightleftharpoons Ni^{IV}_{0.5}Mn^{IV}_{1.5}O_4 + 0.5\,Li^+ + 0.5\,e^-$$

Unlike LNMO with a stoichiometric composition regarding the Mn/Ni ratio (3:1), which typically exhibits a single voltage plateau associated with the Ni^{2+}/Ni^{4+} redox couple, the nonstoichiometric Mn-rich LNMO shows two distinct voltage plateaus, indicating the presence of Mn^{3+}, consistent with the conclusions obtained from XRD refinement in Fig. 3(a). Moreover, in the solid-solution region often a significant decay in smaller particles due to energy dissipation is triggered, driven by the mechanical stress and microstrain originated from differing lattice parameters between coexisting lithium-rich and lithium-poor phases [51].

For a better understanding of the charge-discharge behavior of cells with LNMO cathode and ionic liquid-based electrolytes, Electrochemical Impedance Spectroscopy (EIS) was performed at different cell potentials during the lithium-ion extraction/insertion processes, as shown in Fig. 4 (d) and (e). The measured potential ranges were categorized into the presence of a lithium-poor, the presence of a two-phase equilibrium and lithium-rich phases [52–54]. The resulting Nyquist plots consist of a slightly depressed semicircle, that is shifted along the Z'-axis and a linear tail with an angle of around 45°. These features can be modelled by using a Randles equivalent circuit, see Fig. 4(c). Hereby, the resistance R_e represents most probably the bulk electrolyte, the resistance R_{ct} and the constant phase element Q_{ct} an interphase ionic charge transfer

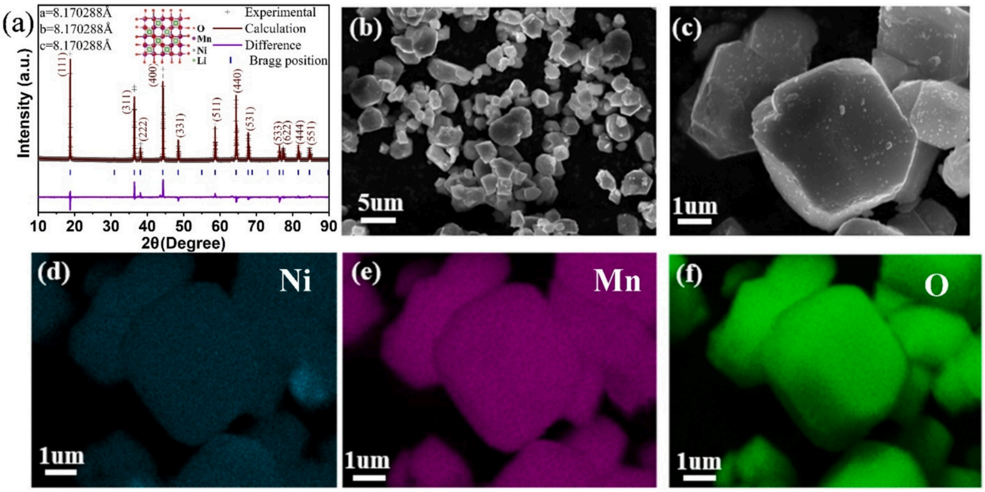

Fig. 3. Structural and morphological characterization of the $LiNi_{0.5}Mn_{1.5}O_4$ (LNMO) cathode. (a) Rietveld refinement of the powder XRD (room temperature); (b, c) micrographs of the LNMO powder taken by scanning electron microscopy (SEM/BSE) at 20 kV accelerating voltage, and (d-f) corresponding Ni, Mn, and O elemental mappings.

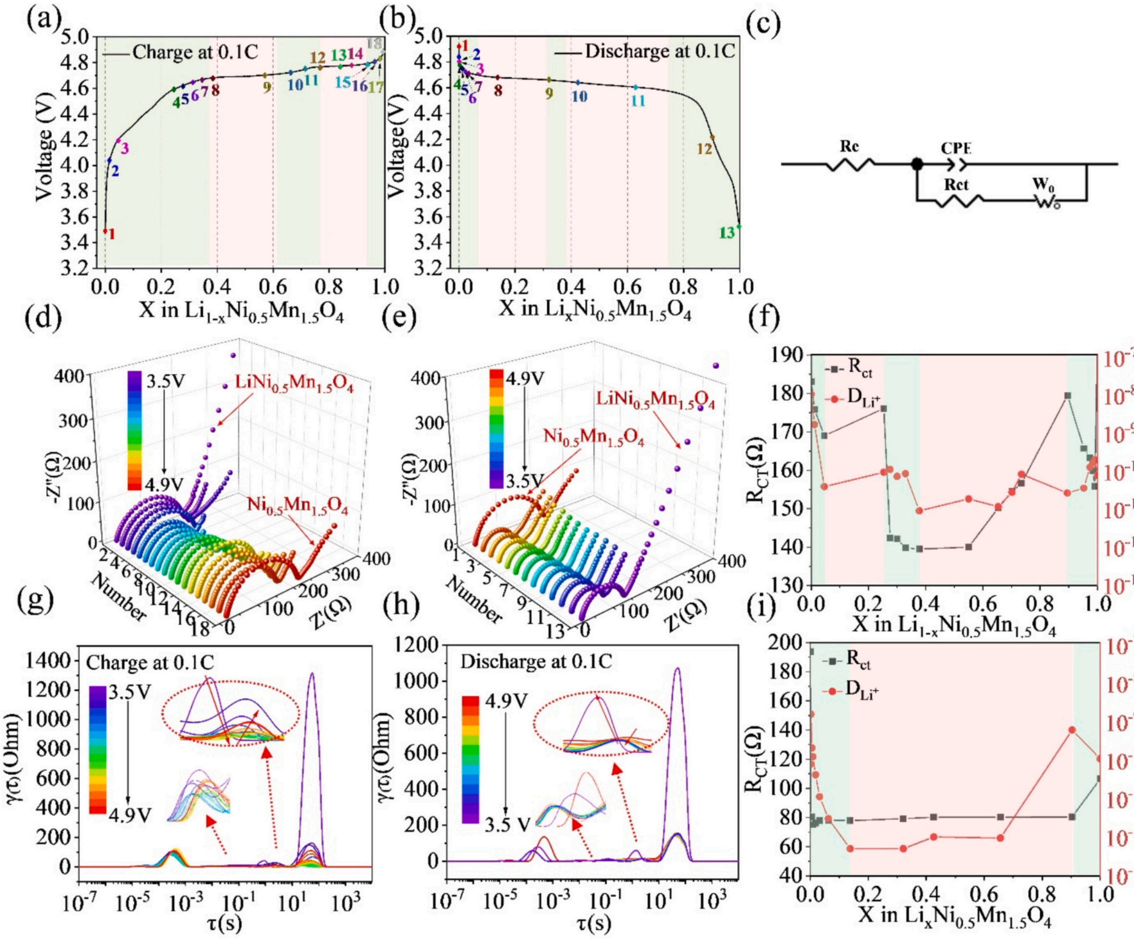

Fig. 4. Electrochemical behavior and phase-dependent kinetics of LNMO using an electrolyte with "anion-rich" Li^+ solvation sheath. The 1st cycle of the (a) charge, and (b) discharge curves in the range 3.5–4.9 V; (c) the equivalent circuit diagram, used for fitting the *in-situ* EIS, and confirmed by DRT analysis at different voltages in 1st charge (d, g) and discharge (e, h) cycle; (f, i) The Li^+ diffusion coefficients correspond to different charge states of LNMO.

process and the Warburg impedance W_0 an diffusional matter transport processes, respectively [55].

As expected, the electrolyte resistance R_e (real part) is nearly constant, only slightly changing from 9.9 to 11.6 Ω during the entire Li^+ insertion/extraction process. The charge transfer resistance R_{ct} and the diffusion coefficient $\widetilde{D}_{Li}$ corresponding to the Warburg impedance W_0 were calculated, plotted in Fig. 4(f, i) and compiled in Tables S2, 3. Considering a negligible variation in lithium-ion concentration within the bulk electrolyte, changes in R_{ct} can be primarily attributed to electrode-side processes. During the charging process, as lithium is deintercalated from the Li-rich to the Li-poor regime at SOC ≈ 0–0.05, 0.25–0.39, and 0.9–1.0, R_{ct} decreases progressively from 183.1 to 169.0 Ω, 176.1 to 139.8 Ω, and 179.5 to 155.9 Ω, respectively (green areas in Fig. 4(f)). This indicates an improved charge-transfer kinetics (exchange current density). In contrast, within the Mn^{3+}/Mn^{4+} and Ni^{2+}/Ni^{4+} two-phase regions at SOC ≈ 0.05–0.25 and 0.39–0.9, it increases from 169.0 to 176.1 Ω and from 139.8 to 179.5 Ω, respectively (pink areas in Fig. 4 (f)). This behavior is also reported in the literature and is attributed to the formation and migration of phase boundaries in the LNMO grains, which introduce lattice strain and structural heterogeneity and impede the ionic charge transport [51]. As the delithiation proceeds beyond the two-phase coexistence region, the system transforms to a single-phase λ-MnO_2, reducing structural mismatch and facilitating improved charge transfer, reflected by the subsequent decrease in R_{ct}.

All impedance spectra were recorded in the frequency range from 100 kHz down to 10 mHz. As shown in Fig. 4(d) and (e), the Warburg impedance in the low-frequency region of the impedance spectrum appears only as a short tail in the two-phase region but as a long straight line in the solid-solution regions, also reflecting two distinct lithium ion diffusion behavior. In the solid-solution phase, lithium ions diffuse uniformly between the surface and the centre of the cathode material particles. In contrast, the shorter response in the two-phase region could be associated with additional kinetic limitations, such as those introduced by the movement of phase boundaries [51,56,57]. The diffusion pathway becomes inhomogeneous—the charge transfer of Li^+ ions across a boundary most probably requires an activation energy, a chemical potential difference will be present at the boundary, leading to slower overall transport kinetics.

The non-monotonic variation of about four orders of magnitude for the diffusion coefficient $\widetilde{D}_{Li}$, calculated from the Warburg impedance, is shown in Fig. 4(f, i). During the 1st charge process, it ranges from $9.38 \bullet 10^{-12}$ to $1.11 \bullet 10^{-8}$ cm^2 s^{-1}, while during the discharge process, it ranges from $5.09 \bullet 10^{-13}$ to $1.63 \bullet 10^{-9}$ cm^2 s^{-1}. The observed diffusion process can be most probably attributed to the chemical diffusion of the component lithium, *i.e.* $\widetilde{D}_{Li}$, in the cathode material during charging and discharging. This is reported in many other studies [58,59]. However, the diffusion coefficients at individual voltages generally exceed those typically reported in the literature by an order of magnitude. This discrepancy may be attributed to surface-related structural or interfacial changes that facilitate lithium-ion transport [60]. The initial drop in $\widetilde{D}_{Li}$ occurs during the early stages of lithium deintercalation coinciding with the Mn^{3+}/Mn^{4+} redox process ($Li_1Ni_{0.5}Mn_{1.5}O_4 \rightarrow Li_xNi_{0.5}Mn_{1.5}O_4$). $\widetilde{D}_{Li}$ diminishes from an initial magnitude of $1.11 \bullet 10^{-8}$ to $9.70 \bullet 10^{-11}$ cm^2

s^{-1}. Further reductions are observed during the Ni^{2+}/Ni^{3+} and Ni^{3+}/Ni^{4+} redox processes, corresponding to approximately 40 % and 90 % lithium deintercalation ($Li_xNi_{0.5}Mn_{1.5}O_4 \rightarrow Ni_{0.5}Mn_{1.5}O_4$), where $\widetilde{D}_{Li}$ drops to $9.38 \bullet 10^{-12}$ and $3.71 \bullet 10^{-11}$ cm^2 s^{-1}, respectively. One possible explanation for this phenomenon is the formation and propagation of multiple phase boundaries during structural phase transitions. Finally, after 97 % of lithium deintercalation, the $\widetilde{D}_{Li}$ value recovers to $2.06 \bullet 10^{-10}$ cm^2 s^{-1}.

This study further utilizes an analysis of the distribution of relaxation times (DRT). The results are depicted in Fig. 4(g) and (h). Generally, ion transport and electrochemical reactions do not manifest at high frequencies. Therefore, in the DRT plot, the five areas associated with the time constant τ from large to small represent the mass transfer process ($\tau \approx 10^2$ s, $f \approx 15.9$ mHz), charge transfer process ($\tau \approx 10^0$ s, $f \approx 0.16$ Hz), cathode/electrolyte layer resistance ($\tau \approx 10^{-2}$ s, $f \approx 15.9$ Hz), anode/electrolyte layer resistance ($\tau \approx 10^{-3}$ s, $f \approx 0.16$ kHz), and contact resistance ($\tau \approx 10^{-5}$ s, $f \approx 15.9$ kHz), respectively [61,62]. The region with time constants ranging from 10^0 to 10^2 is notably influenced by changes in the state of charge (SOC). This region corresponds to the charge transfer resistance R_{ct} and Warburg impedance in the equivalent circuit. However, due to limitations in circuit fitting, no R–CPE element corresponding to the remaining three DRT time constants were resolved in the equivalent circuit. As the SOC decreases, the time constants in this region generally increase, while the corresponding intensity progressively weakens. A similar intensity trend is observed during discharge process. However, at low SOC levels, this behavior reverses, with the intensity increasing once again. This pattern aligns with the trends seen in the EIS plots and the variation of Li^+ charge transfer resistance.

3.2.3. Battery performance

To further estimate the electrochemical behaviors of our ionic liquid electrolyte, a half cell composed with Li anode and LNMO cathode was fabricated and measured. The rate capabilities and cycle performance of Li||LNMO cells using the LP30 and the PLF-3M-0.3B electrolyte at a rate of 0.5, 0.8, 1.0, 1.5, and 0.2C, respectively were shown in Fig. 5(a). As expected, employing the LP30 electrolyte exhibits a cycle life (30.68 % retention of the initial capacity) of only 70 cycles after a rate test. When PLF-3M-0.3B was employed as electrolyte, the LNMO||Li cells cycle life was improved. The specific capacity of LNMO decreases from the initial 123.9 to 104.2 mAh/g at around 100th after rate test, showing a remarkable capacity retention of 84.1 %. Additionally, the LNMO electrode with the PLF-3M-0.3B electrolyte demonstrates excellent rate performance, delivering capacities of 119.5, 107.4, 95.3, and 61.9 mAh/g at current densities of 0.5, 0.8, 1.0, and 1.5C, respectively. When the current density returns to 0.2C, the capacity recovers to 122.8 mAh/g. In contrast, the LNMO electrode with the LP30 electrolyte retains only 98.8 mAh/g at 0.2C and rapidly degrades due to its instability under high applied voltage. Fig. 5(b) shows the charge/discharge profiles of the Li||LNMO cells using the PLF-3M-0.3B electrolyte at different cycles. The formation of electrode/electrolyte film during the activation process causes a low coulombic efficiency (87.56 %) for the first cycle. During the subsequent charge and discharge process, the charge/discharge ratio continues to rise and remains above 98 %. The typical dQ/dV curves of LNMO for the 1st, 7th, and 10th cycles, shown in Fig. 5(c), indicate that the primary redox process associated with Ni^{2+}/Ni^{4+} occurs at approximately 4.69 V. With increasing cycle number, the oxidation-reduction peak area associated with the Ni^{2+}/Ni^{4+} decreases, corresponding to a gradual capacity fade consistent with the trend observed in the Fig. 5(a-c). Additionally, The dQ/dV curves show progressive separation of the Ni^{2+}/Ni^{3+} and Ni^{3+}/Ni^{4+} redox peaks with cycling.

3.3. The cathode electrolyte interphase

3.3.1. HOMO-LUMO characteristics and XPS analysis

To elucidate the decomposition tendency of each component in the electrolyte, density functional theory (DFT) calculations were performed to obtain the highest occupied molecular orbital (HOMO) and lowest unoccupied molecular orbital (LUMO) energy levels of the individual solvent molecules and ions. The HOMO and LUMO energies and their gaps are given in Fig. 6(a). The HOMO energy levels of these species follow the order: $Pyr_{14}^+ < BTFE < FSI^-$, implying that FSI^- is most readily oxidized. As shown in Fig. 6(a), the HOMO of FSI^- is

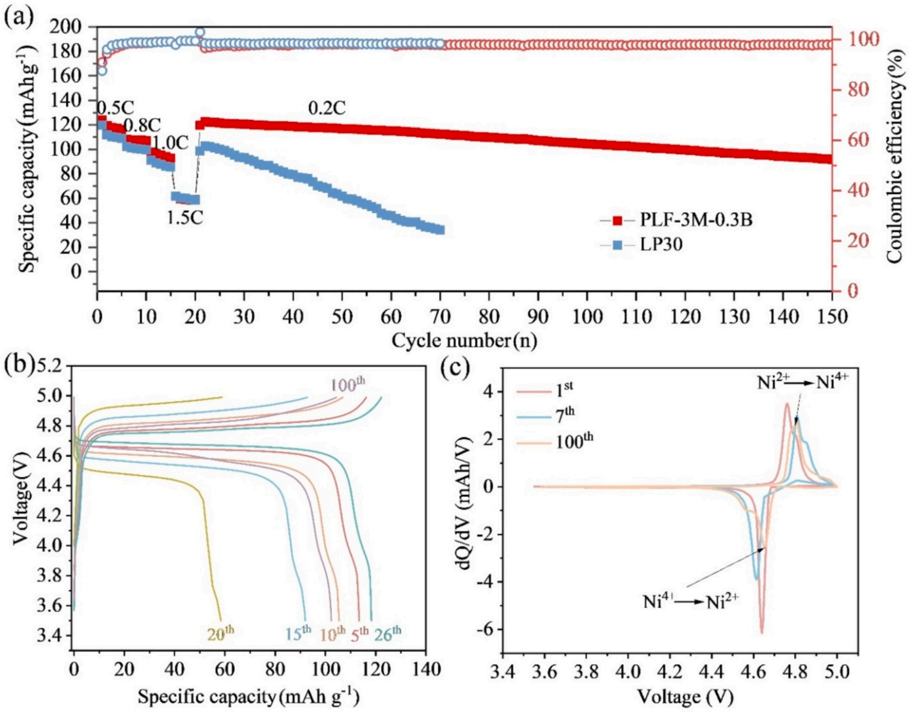

Fig. 5. Rate and cycling performance of the Li||LNMO cells employing the PLF-3M-0.3B ionic liquid electrolyte. (a) Rate performance and cycling retention at 0.5–1.5C and return to 0.2C; (b) charge/discharge profiles after 5th, 10th, 15th, 20th, 26th, and 100th cycles; (c) dQ/dV curves of the 1st, 7th, and 100th cycles.

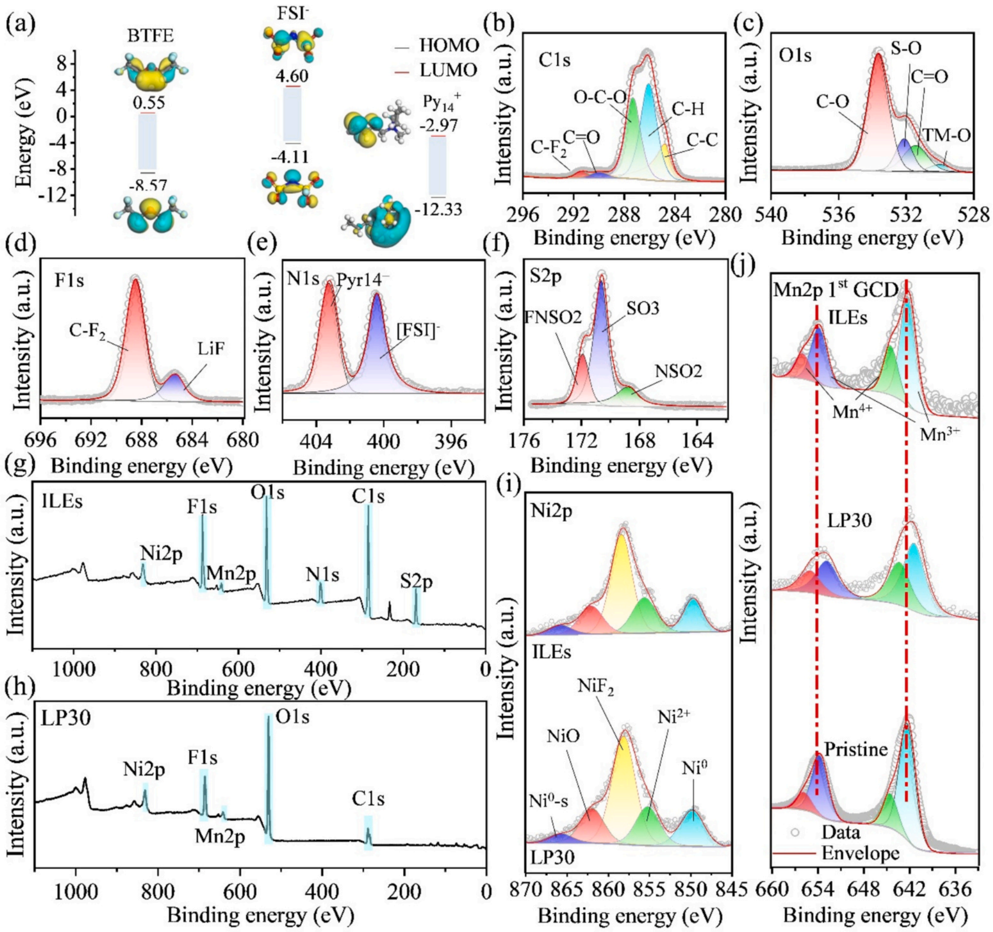

Fig. 6. HOMO-LUMO characteristics and interphase composition of LNMO after cycling in different electrolytes. (a) HOMO-LUMO energy levels of the species present in the ionic liquid electrolyte; XPS spectra of an LNMO cathode after initial cycling in a Li^+ electrolyte with an anion-rich solvation sheath at (b) C1s, (c) O1s, (d) F1s, (e) N1s, (f) S2p, (g, h) survey spectra, (i) Ni2p, and (j) Mn2p.

primarily localized on the highly electronegative fluorine atoms, while that of BTFE is mainly distributed over the oxygen atoms.

To further examine the composition of a cathode electrolyte interphase (CEI), possibly formed on the surface of the LNMO cathode before and after initial cycling in a Li^+ electrolyte with anion-rich solvation sheath, X-ray photoelectron spectroscopy (XPS) survey scans were conducted. The C1s and O1s core level peaks are depicted in Fig. 6(b) and (c). The C1s peak can be deconvoluted into five components: 1) at 284.8 eV assigned to C—C (Super P), 2) at 286.05 eV assigned to C—H bonds (PVDF), 3) at 287.28 eV assigned to O-C-O bonds of BTFE, 4) at 289.96 eV assigned to C═O, and 5) at 291.36 eV assigned to C—F_2 bonds (PVDF) [63]. Notably, a significant presence of O-C-O groups in the C1s spectra can be observed compared to both pristine LNMO and LNMO after cycling in an LP30 electrolyte (Supporting information Figs. S6(a) and S7(a)), arising from the decomposition of BTFE. The O1s core level peak consists of four components: 1) at 530.0 eV assigned to Mn—O bonds, 2) at 531.41 eV assigned to C═O and Mn-OH bonds, 3) at 532.08 eV assigned to S—O bonds, and 4) at 533.64 eV assigned to C—O bonds. A notable presence of SO_2 moieties is observed in the O1s spectra, most probably originating from the decomposition of FSI^- anions [64,65]. Fig. 6(d) and (e) shows the deconvoluted F1s and N1s peaks, respectively. After initial cycling in a cell employing an LNMO cathode and a Li^+ electrolyte with and anion-rich solvation sheath, two peaks are observed in the F1s spectrum of the LNMO cathode material at 685.28 eV and 688.47 eV, attributed to the Li—F, and C—F bonds originating from LiF, and the polyvinylidene difluoride (PVDF) binder, respectively [65]. LiF, formed immediately after intial cycling, tends to precipitate easily on the surface of the cathode active materials, thereby forming resistive layers that impede electronic conduction but still allow ionic charge transport. In contrast, Fig. S7(c) shows that the composition of the LNMO surface after cycling in LP30 is primarily dominated by $Li_xPO_yF_z$ [66]. The N1s peak was also fitted by two components: 1) at 400.37 eV assigned to the FSI^- anion and 2) at 403.23 eV assigned to the Pyr_{14}^+ cation. For pristine LNMO and LNMO after cycling in an LP30 electrolyte (Figs. S6 and S7(d)), no characteristic peaks could be observed. Fig. 6(f-h) shows the deconvoluted S2p and survey spectra of the LNMO cathode after initial cycling. The core level peak of S2p consists of three components: 1) at 168.65 eV to be assigned to NSO_2, 2) at 170.58 eV to be assigned to SO_3 bonds, and 3) 171.84 eV to be assigned to $FNSO_2$. Both the O1s peak at 532.08 eV and the S2p peaks at 168.65 and 171.84 eV represent the presence of SO_2 moieties, which is considered to be an influential functional group for enhancing the surface stability of cathodes [67,68]. This moiety facilitates the migration of Li^+ ions by the partial negative charge of oxygen atoms while inhibiting electron transfer at the electrode-electrolyte interphase, thereby suppressing electrolyte decomposition during cycling. In addition, the XPS survey spectrum also reveals no detectable signals of S or N elements on the surface of the LNMO electrode after cycling in an LP30 electrolyte, suggesting the absence of S- or N-containing functional groups in the surface layer.

The Ni2p and Mn2p core-level spectra of the LNMO surface after cycling are depicted in Fig. 6(i, j). Five distinct Ni2p peaks were identified by deconvolution. The peak at 861.87 eV can be attributed to NiO, which is likely formed as a result of side reactions between dissolved

Ni^{2+} ions and the electrolyte [69]. The peak at 858.04 eV corresponds to the binding energy of Ni—F bonds in NiF_2, suggesting a reaction between dissolved Ni^{2+} ions and fluorinated electrolyte components [66,70,71]. Additionally, the peaks at 849.80 and 865.75 eV are assigned to Ni^0, consistent with reports on other Ni-containing electrode systems [66,71]. The peak centered at approximately 855.12 eV is characteristic of Ni^{2+} species [72,73]. Notably, the relative area of this Ni^{2+} peak is 18.57 % for the sample cycled in the ionic liquid electrolyte, compared to 17.14 % for that in LP30, implying that the ionic liquid electrolyte helps maintain a higher fraction of Ni^{2+} and may suppress parasitic side reactions. Furthermore, the LNMO cathode shows a slightly lower NiO fraction after cycling in the ionic liquid electrolyte (14.76 %) than in LP30 (15.23 %). The Mn^{3+} $2p_{3/2}$ and $2p_{1/2}$ peaks are located at 642.24 eV and 653.65 eV, while the Mn^{4+} $2p_{3/2}$ and $2p_{1/2}$ peaks appear at 644.46 eV and 655.82 eV, respectively. The peak position in the Mn2p spectra remains unchanged, indicating that the dissolution of Mn by acidic media at a high cut-off voltage did not occur [74]. A stable CEI layer formed at the electrode/electrolyte interphase effectively inhibits this process from occurring.

3.3.2. *TEM investigations*

TEM, HRTEM and SAED images of LNMO particles from the cathode after the first GCD measurement in the coin cell are shown in Fig. 7(a-d), revealing the maintenance of its micrometer-level polyhedral shape. After the galvanostatic charge/discharge test, the sample still maintains a sharp surface and edges, which can be clearly depicted in the dark area of Fig. 7(a). It can be concluded that it still exhibits high crystallinity and has a polyhedral shape. The corresponding Fast Fourier transform (FFT) of this image region in Fig. 7(b) clearly displays the symmetric pattern, also indicating the high crystallinity. Additionally, the HRTEM images of LNMO in Fig. 7(b, c) show the formation of a CEI film with a thickness of approximately 0.8 nm on the surface of the cathode material. According to the results from XPS spectroscopy, the CEI layer is most likely composed of LiF, the decomposition products of FSI^- anions and SO_2 moieties, resulting from the synergistic effect of the Li^+ special solvation sheath and the co-solvent BTFE. The robust CEI film, formed during the initial charging/discharging process, promotes an inorganic-rich interphase that mitigates parasitic reactions. [74–76].

Fig. 7(d) shows a SAED pattern of an entire particle with all diffraction rings corresponding to the spinel-type LNMO. The fringe spacings in Fig. 7(d) of 0.47, 0.29, 0.25, and 0.17 nm correspond to (111), (220), (311), and (422) lattice planes of LNMO [77], respectively, further confirming the preserved spinel structure and demonstrating the crystal framework remains stable under high voltage or cation impact.

3.3.3. *Consequences for the cation solvation at different electrolyte concentrations*

Fig. 8(a) depicts the solvation of Li^+ in conventional molecular solvent-based electrolytes at various salt concentrations. In diluted systems, mainly neutral solvent molecules are in the solvation sheath of the Li^+ cations. The anions are not in direct contact, but separated by the dielectric solvent molecules (solvent separated ion pairs, SSIP). At higher electrolyte concentrations, the number of solvent molecules does not allow a full separation of the ions. This results in an increasing number of anions in the inner Li^+ solvation sheath (contact ion pairs, CIP). CIP-type electrolytes reach oversaturated states post-desolvation, gradually diminishing the benefits of high electrolyte concentration. Ultimately, the proportion of anions coordinating the Li^+ solvation

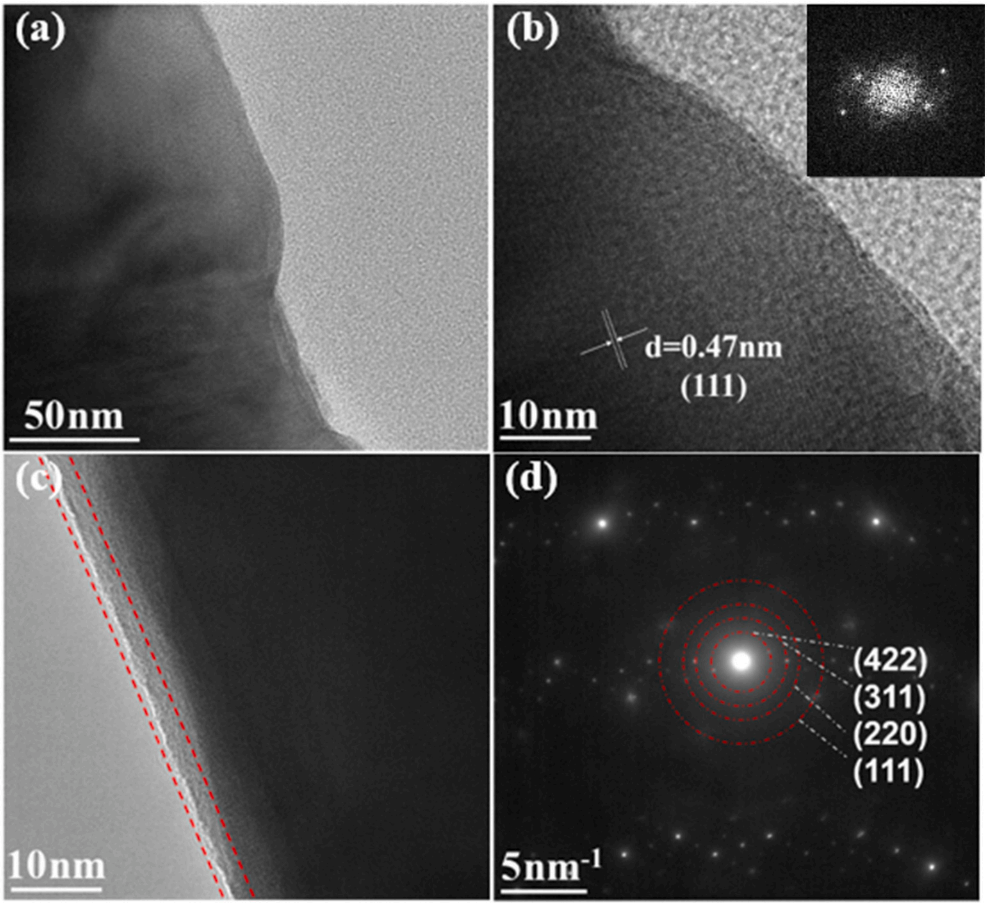

Fig. 7. Microstructural evolution of LNMO and formation of CEI after initial cycling in the anion-rich electrolyte. (a) TEM, (b, c) HRTEM, and (d) Selected Area Electron Diffraction (SAED) pattern.

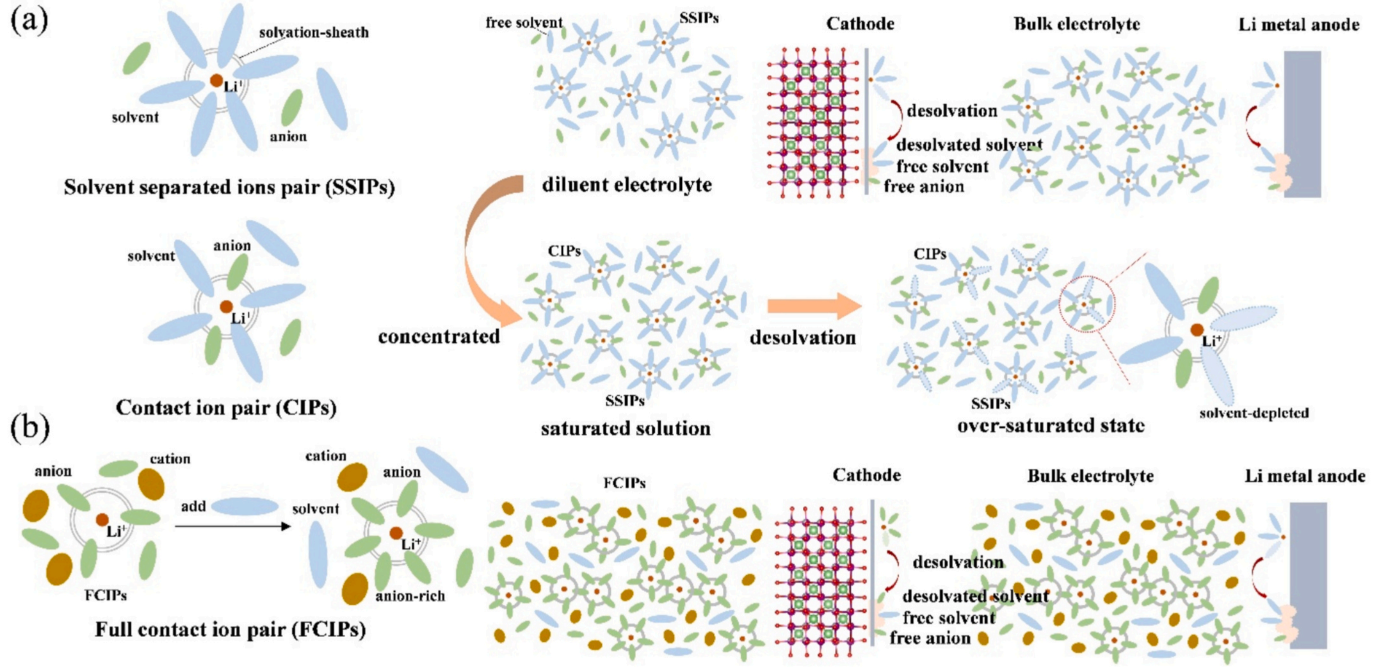

Fig. 8. (a) Solvent-separated ions pair (SSIPs), contact ion pair (CIPs) solvation structure and associated decomposition issues in high-voltage lithium metal battery; (b) full contact ion pair (FCIPs) solvation sheath of Li^+ in ionic liquid-based electrolyte and its unlimited replenish process.

sheath reaches saturation, constrained by the lithium salts' solubility limit.

The solvation structure of the Li^+ cations in electrolytes using ionic liquids as solvents, as shown in Fig. 8(b), is composed entirely of anions and exclusively utilizes anions during the desolvation process at the electrode interface. Concurrently, free solvent molecules and anions contribute to the formation of the electrode/electrolyte interphase. Additionally, as shown in Fig. 8(b), the inclusion of a co-solvent increases the number of anions in the Li^+ solvation sheath, *i.e.* increases the fraction of Li^+ coordinated anions to free anions, allowing more anions from the solvent sheaths to contribute to the electrode/electrolyte interphase formation.

4. Conclusion

We investigated Li^+ electrolytes, based on an ionic liquid as solvent with an anion-rich solvation sheath, respectively full-contact-ion-pairs (FCIP), by adjusting the ratio of a molecular co-solvent, *i.e.* bis-(2,2,2-trifluoroethyl)ether (BTFE) as a new approach to gain a better compatibility to future high voltage cathode materials. An FTIR and Raman analysis suggests, that the introduction of the co-solvent BTFE results in a denser packing of FSI^- anions around Li^+ cations, forming a distinctive anion-rich Li^+ solvation structure, with a fraction of Li^+-coordinated FSI^-: corrdinated FSI^- exceeding 90 %. The fraction of Li^+-coordinated FSI is increasing from 0.6 to 0.91 due to the interaction with the co-solvent bis-(2,2,2-trifluoroethyl)ether, while it did not occupy the first solvation sheath of Li^+.

This approach improves the electrolyte viscosity and wettability. Moreover, it is allowing more anions to participate in the formation of a cathode/electrolyte interphase (CEI). In the presence of anion-rich Li^+ solvation structures and bis-(2,2,2-trifluoroethyl)ether, a $LiNi_{0.5}Mn_{1.5}O_4$ (LNMO) cathode forms a robust CEI, predominantly composed of LiF, SO_3 functional groups, and the decomposition products of 1-Butyl-1-methylpyrrolidinium cations, which effectively inhibits the dissolution of Mn ions. Moreover, IL-based solvents exhibit a wider electrochemical window compared to conventional alkylcarbonate solvents.

In addition, *in-situ* impedance spectroscopy and galvanostatic charge-discharge plots were used to investigate the relationship between the lithium stripping process and the phase transition of the LNMO cathode. During the Ni^{2+}/Ni^{3+} and Ni^{3+}/Ni^{4+} redox processes, accompanied with phase transitions (($LiNi_{0.5}Mn_{1.5}O_4 \rightarrow Li_{0.5}Ni_{0.5}Mn_{1.5}O_4 \rightarrow Ni_{0.5}Mn_{1.5}O_4$), the diffusion coefficient $\widetilde{D}_{Li}$ of the component Li decreases to $9.38 \bullet 10^{-12}$ and $3.71 \bullet 10^{-11}$ $cm^2\ s^{-1}$, respectively. TEM and XPS results confirms the assumption that the enhancement in the coordination number of FSI^- anions surrounding Li^+, coupled with the co-solvent BTFE, confers a stable LiF protective layer upon LNMO cathodes during operation. The unique anion-rich FCIP solvation structure enables a high-voltage LNMO cathode with a low interfacial resistance while exhibiting an enhanced electrode Li^+ diffusion coefficient. This study enhances the understanding of how fluoro-ether solvents like bis-(2,2,2-trifluoroethyl)ether influence the coordination of Li^+ cations by anions. It also highlights that Li^+ electrolytes based on ionic liquids (IL) with an anion-rich solvation structure tends to form a robust cathode electrolyte interphase (CEI) in $LiNi_{0.5}Mn_{1.5}O_4$. This research contributes to a new electrolyte designs and future application of high-Mn cathode materials, exemplified by the 5 V voltage $LiNi_{0.5}Mn_{1.5}O_4$.

CRediT authorship contribution statement

Yuanbo Chen: Writing – review & editing, Writing – original draft, Methodology, Investigation, Conceptualization. **Kai Yao:** Writing – review & editing, Software, Methodology. **Wei Qin:** Methodology, Investigation. **Christian Rodenbücher:** Writing – review & editing. **Jiangshui Luo:** Writing – review & editing, Software, Resources. **Carsten Korte:** Writing – review & editing, Supervision, Resources, Project administration.

Declaration of competing interest

We declare that this manuscript is original, has not been published before and is not currently being considered for publication elsewhere.

The authors declare that they have no known competing financial interests or personal relationships that could have appeared to influence the work reported in this paper.

Acknowledgements

This work is partially supported by the China Scholarship Council (Grant No: 202206240006). J. Luo acknowledges National Natural Science Foundation of China (project No.: 22378270 and 21776120), Sichuan Science and Technology Program (project No.: 2023JDRC0013), Hohhot Science and Technology Program (project No.: 2023-JieBangGuaShuai-Gao-3) and Natural Science Foundation of Fujian Province, China (project No.: 2023J01254). We appreciate the Analytical – Testing Center of Sichuan University for providing Materials Studio and Institute of Energy Materials and Devices (IMD-2) for the help of TGA measurements. The authors are thankful to Ceshigo Research Service (www.ceshigo.com) for providing the TEM and XPS testing service. All authors are grateful for the support of the Helmholtz Association.

Appendix A. Supplementary data

Supplementary data to this article can be found online at https://doi.org/10.1016/j.est.2025.120193.

Data availability

Data will be made available on request.

References

[1] J. Xu, X. Cai, S. Cai, et al., High-energy lithium-ion batteries: recent progress and a promising future in applications, Energy Environ. Mater. 6 (2023) e12450.

[2] A. Innocenti, D. Bresser, J. Garche, et al., A critical discussion of the current availability of lithium and zinc for use in batteries, Nat. Commun. 15 (2024) 4068.

[3] X. Shen, H. Liu, X. Cheng, et al., Beyond lithium ion batteries: higher energy density battery systems based on lithium metal anodes, Energy Storage Mater. 12 (2018) 161–175.

[4] J. Liu, Z. Bao, Y. Cui, et al., Pathways for practical high-energy long-cycling lithium metal batteries, Nat. Energy 4 (2019) 180–186.

[5] S. Kim, G. Park, S. Lee, et al., Lithium-metal batteries: from fundamental research to industrialization, Adv. Mater. 35 (2023) 2206625.

[6] Y. Huang, Y. Dong, S. Li, et al., Lithium manganese spinel cathodes for lithium-ion batteries, Adv. Energy Mater. 11 (2021) 2000997.

[7] J. Xiang, Y. Wei, Y. Zhong, et al., Building practical high-voltage cathode materials for lithium-ion batteries, Adv. Mater. 34 (2022) 2200912.

[8] S. Jiao, X. Ren, R. Cao, et al., Stable cycling of high-voltage lithium metal batteries in ether electrolytes, Nat. Energy 3 (2018) 739–746.

[9] X. Ren, L. Zou, X. Cao, et al., Enabling high-voltage lithium-metal batteries under practical conditions, Joule 3 (2019) 1662–1676.

[10] Y. Chen, W. Qin, J. An, et al., Island-like MoO_{3-x} film grown on Mo foil as high-performance lithium-ion battery anode: a new strategy for preparing flexible electrode, J. Mater. Sci. 57 (2022) 5552–5565.

[11] W. Qin, Y. Chen, J. An, et al., Self-supported $Li_4Ti_5O_{12}$ nanobelt array anode with long-life and improved low-temperature performance for flexible lithium-ion batteries, Ceram. Int. 48 (2022) 22153–22162.

[12] W. Chen, H. Hsieh, D. Wu, et al., Advanced TiO_2/Al_2O_3 bilayer ALD coatings for improved lithium-rich layered oxide electrodes, ACS Appl. Mater. Interfaces 16 (2024) 13029–13040.

[13] W. Qin, Y. Chen, J. An, et al., 3D N-doped $Li_4Ti_5O_{12}$ nanoribbon networks self-supported on Ti foils as advanced anode for high-performance flexible lithium-ion batteries, J. Alloys Compd. 910 (2022) 164873.

[14] Y. Ugata, K. Shigenobu, R. Tatara, et al., Solvate electrolytes for Li and Na batteries: structures, transport properties, and electrochemistry, Phys. Chem. Chem. Phys. 23 (2021) 21419–21436.

[15] Z. Chang, Y. Qiao, H. Deng, et al., A liquid electrolyte with de-solvated lithium ions for lithium-metal battery, Joule 4 (2020) 1776–1789.

[16] Q. Wu, M. McDowell, Y. Qi, Effect of the electric double layer (EDL) in multicomponent electrolyte reduction and solid electrolyte interphase (SEI) formation in lithium batteries, J. Am. Chem. Soc. 145 (2023) 2473–2484.

[17] Z. Sun, J. Yang, H. Xu, et al., Enabling an inorganic-rich interface via cationic surfactant for high-performance lithium metal batteries, Nano Micro Lett. 16 (2024) 141.

[18] Y. Yamada, J. Wang, S. Ko, et al., Advances and issues in developing salt-concentrated battery electrolytes, Nat. Energy 4 (2019) 269–280.

[19] X. Gao, F. Wu, A. Mariani, et al., Concentrated ionic-liquid-based electrolytes for high-voltage lithium batteries with improved performance at room temperature, ChemSusChem 12 (2019) 4185–4193.

[20] X. Wang, M. Salari, D. Jiang, et al., Electrode material–ionic liquid coupling for electrochemical energy storage, Nat. Rev. Mater. 5 (2020) 787–808.

[21] Y. Zheng, D. Wang, S. Kaushik, et al., Ionic liquid electrolytes for next-generation electrochemical energy devices, EnergyChem 4 (2022) 100075.

[22] Q. Liu, W. Jiang, M.J.P. Munoz, et al., Stabilized electrode/electrolyte interphase by a saturated ionic liquid electrolyte for high-voltage NMC532/Si-graphite cells, ACS Appl. Mater. Interfaces 12 (2020) 23035–23045.

[23] T. Yamamoto, T. Nohira, Amide-based ionic liquid electrolytes for alkali-metal-ion rechargeable batteries, Chem. Rec. 23 (2023) e202300169.

[24] N. Sánchez-Ramírez, B.D. Assresahegn, D. Bélanger, et al., A comparison among viscosity, density, conductivity, and electrochemical windows of N-n-butyl-N-methylpyrrolidinium and triethyl-n-pentylphosphonium bis(fluorosulfonyl imide) ionic liquids and their analogues containing bis(trifluoromethylsulfonyl) imide anion, J. Chem. Eng. Data 62 (2017) 3437–3444.

[25] Z. Jusys, M. Binder, J. Schnaidt, et al., A novel DEMS approach for studying gas evolution at battery-type electrode/electrolyte interfaces: high-voltage $LiNi_{0.5}Mn_{1.5}O_4$ cathode in ethylene and dimethyl carbonate electrolytes, Electrochim. Acta 314 (2019) 188–201.

[26] G.M. Hobold, A. Khurram, B.M. Gallant, et al., Operando gas monitoring of solid electrolyte interphase reactions on lithium, Chem. Mater. 32 (2020) 2341–2352.

[27] D. Wang, A. Xiao, L. Wells, et al., Effect of mixtures of lithium hexafluorophosphate ($LiPF_6$) and lithium bis(fluorosulfonyl)imide (LiFSI) as salts in $Li[Ni_{1/3}Mn_{1/3}Co_{1/3}]O_2$/graphite pouch cells, J. Electrochem. Soc. 162 (2014) A169–A175.

[28] J. Alvarado, M.A. Schroeder, M. Zhang, et al., A carbonate-free, sulfone-based electrolyte for high-voltage Li-ion batteries, Mater. Today 21 (2018) 341–353.

[29] I.A. Shkrob, T.W. Marin, Y. Zhu, et al., Why bis(fluorosulfonyl)imide is a “magic anion” for electrochemistry, J. Phys. Chem. C 118 (2014) 19661–19671.

[30] X. Ren, P. Gao, L. Zou, et al., Role of inner solvation sheath within salt-solvent complexes in tailoring electrode/electrolyte interphases for lithium metal batteries, PNAS 117 (2020) 28603–28613.

[31] T.D. Pham, A.B. Faheem, J. Kim, et al., Practical high-voltage lithium metal batteries enabled by tuning the solvation structure in weakly solvating electrolyte, Small 18 (2022) 2107492.

[32] B. Yang, C. Li, J. Zhou, et al., Pyrrolidinium-based ionic liquid electrolyte with organic additive and LiTFSI for high-safety lithium-ion batteries, Electrochim. Acta 148 (2014) 39–45.

[33] H. Tu, L. Li, Z. Wang, et al., Tailoring electrolyte solvation for LiF-rich solid electrolyte interphase toward a stable Li anode, ACS Nano 16 (2022) 16898–16908.

[34] L. Yu, S. Chen, H. Lee, et al., A localized high-concentration electrolyte with optimized solvents and lithium difluoro(oxalate)borate additive for stable lithium metal batteries, ACS Energy Lett. 3 (2018) 2059–2067.

[35] S. Chen, J. Zheng, D. Mei, et al., High-voltage lithium-metal batteries enabled by localized high-concentration electrolytes, Adv. Mater. 30 (2018) e1706102.

[36] M. Ono, S. Matsuda, Lithium nitrate/amide-based localized high concentration electrolyte for rechargeable lithium–oxygen batteries under high current density and high areal capacity conditions, ACS Appl. Energy Mater. 6 (2023) 3357–3365.

[37] J.P. Perdew, K. Burke, M. Ernzerhof, Generalized gradient approximation made simple, Phys. Rev. Lett. 77 (1996) 3865–3868.

[38] L.G. Chagas, S. Jeong, I. Hasa, et al., Ionic liquid-based electrolytes for sodium-ion batteries: tuning properties to enhance the electrochemical performance of manganese-based layered oxide cathode, ACS Appl. Mater. Interfaces 11 (2019) 22278–22289.

[39] L. Nyholm, T. Ericson, A.S. Etman, Revisiting the stability of aluminum current collectors in carbonate electrolytes for high-voltage Li-ion batteries, Chem. Eng. Sci. 282 (2023) 119346.

[40] W.G. Kidanu, L. Munkhaugen, C. Lian, et al., On the moisture tolerance of LiFSI based lithium-ion batteries: a systematic study on NMC622/graphite full cells, Electrochim. Acta 508 (2024) 145213.

[41] V.L. Orkin, E. Villenave, R.E. Huie, et al., Atmospheric lifetimes and global warming potentials of hydrofluoroethers: reactivity toward OH, UV spectra, and IR absorption cross sections, J. Phys. Chem. A 103 (1999) 9770–9779.

[42] N. Oyaro, S.R. Sellevåg, C.J. Nielsen, Study of the OH and Cl-initiated oxidation, IR absorption cross-section, radiative forcing, and global warming potential of four C4-hydrofluoroethers, Environ. Sci. Technol. 38 (2004) 5567–5576.

[43] J.K. Ruff, The imidodisulfuryl fluoride ion, Inorg. Chem. 4 (1965) 1446–1449.

[44] L.J. Hardwick, J.A. Saint, I.T. Lucas, et al., FTIR and Raman study of the $Li_xTi_yMn_{1-y}O_2$ (y=0, 0.11) cathodes in methylpropyl pyrrolidinium bis (fluorosulfonyl) imide, LiTFSI electrolyte, J. Electrochem. Soc. 156 (2008) A120.

[45] J. Huang, A.F. Hollenkamp, Thermal behavior of ionic liquids containing the FSI anion and the Li^+ cation, J. Phys. Chem. C 114 (2010) 21840–21847.

[46] M. Beran, J. Příhoda, Z. Žák, et al., A new route to the syntheses of alkali metal bis (fluorosulfuryl) imides: crystal structure of $LiN(SO_2F)_2$, Polyhedron 25 (2006) 1292–1298.

[47] Y. Umebayashi, T. Mitsugi, S. Fukuda, et al., Lithium ion solvation in room-temperature ionic liquids involving bis (trifluoromethanesulfonyl) imide anion studied by Raman spectroscopy and DFT calculations, J. Phys. Chem. B 111 (2007) 13028–13032.

[48] H. Yoon, A.S. Best, M. Forsyth, et al., Physical properties of high Li-ion content N-propyl-N-methylpyrrolidinium bis(fluorosulfonyl)imide based ionic liquid electrolytes, Phys. Chem. Chem. Phys. 17 (2015) 4656–4663.

[49] J. Zeng, K. Wu, N. Li, et al., Revisiting the temperature-dependent phase structure of spinel $LiNi_{0.5}Mn_{1.5}O_4$ for lithium-ion batteries, ACS Appl. Energy Mater. 7 (2024) 2405–2415.

[50] B.H. Toby, R factors in Rietveld analysis: how good is good enough? Powder Diffract. 21 (2006) 67–70.

[51] S. Kuppan, Y. Xu, Y. Liu, et al., Phase transformation mechanism in lithium manganese nickel oxide revealed by single-crystal hard X-ray microscopy, Nat. Commun. 8 (2017) 1–10.

[52] E. Lee, K.A. Persson, Solid-solution Li intercalation as a function of cation order/disorder in the high-voltage $Li_xNi_{0.5}Mn_{1.5}O_4$ spinel, Chem. Mater. 25 (2013) 2885–2889.

[53] H. Komatsu, H. Arai, Y. Koyama, et al., Solid solution domains at phase transition front of $Li_xNi_{0.5}Mn_{1.5}O_4$, Adv. Energy Mater. 5 (2015) 1500638.

[54] I. Martens, N. Vostrov, M. Mirolo, et al., Defects and nanostrain gradients control phase transition mechanisms in single crystal high-voltage lithium spinel, Nat. Commun. 14 (2023) 6975.

[55] S. Buller, M. Thele, E. Karden, et al., Impedance-based non-linear dynamic battery modeling for automotive applications, J. Power Sources 113 (2003) 422–430.

[56] X.H. Ma, B. Kang, G. Ceder, High rate micron-sized ordered $LiNi_{0.5}Mn_{1.5}O_4$, J. Electrochem. Soc. 157 (2010) A925.

[57] P. Stüble, V. Mereacre, H. Geßwein, et al., On the composition of $LiNi_{0.5}Mn_{1.5}O_4$ cathode active materials, Adv. Energy Mater. 13 (2023) 2203778.

[58] R. Amin, I. Belharouk, M. Ba, Part I: electronic and ionic transport properties of the ordered and disordered $LiNi_{0.5}Mn_{1.5}O_4$ spinel cathode, J. Power Sources 348 (2017) 311–317.

[59] A. Rahim, M. Kufian, A. Arof, et al., Variation of Li diffusion coefficient during delithiation of spinel $LiNi_{0.5}Mn_{1.5}O_4$, J. Electrochem. Sci. Technol. 13 (2022) 128–137.

[60] C. Lin, J. Yin, S. Cui, et al., Improved electrochemical performance of spinel $LiNi_{0.5}Mn_{1.5}O_4$ cathode materials with a dual structure triggered by LiF at low calcination temperature, ACS Appl. Mater. Interfaces 15 (2023) 16778–16793.

[61] J.P. Schmidt, T. Chrobak, M. Ender, et al., Studies on $LiFePO_4$ as cathode material using impedance spectroscopy, J. Power Sources 196 (2011) 5342–5348.

[62] R. Huang, X. Wang, B. Jiang, et al., Revealing the electrochemical impedance characteristics of lithium-ion battery (nickel-cobalt-aluminum vs. graphite) under various alternating current amplitudes, J. Power Sources 566 (2023) 232929.

[63] E.R. Østli, A. Mathew, J.R. Tolchard, et al., Stabilizing the cathode interphase of LNMO using an ionic-liquid based electrolyte, Batteries Supercaps 6 (2023) e202300085.

[64] J. Alvarado, M.A. Schroeder, M. Zhang, et al., A carbonate-free, sulfone-based electrolyte for high-voltage Li-ion batteries, Mater. Today 21 (2018) 341–353.

[65] X. Zhang, X. Chen, L. Hou, et al., Regulating anions in the solvation sheath of lithium ions for stable lithium metal batteries, ACS Energy Lett. 4 (2019) 411–416.

[66] M. Jiang, Q. Zhang, D. Danilov, et al., Formation of a stable solid-electrolyte interphase at metallic lithium anodes induced by $LiNbO_3$ protective layers, ACS Appl. Energy Mater. 4 (2021) 10333–10343.

[67] T. Yi, J. Mei, Y. Zhu, Key strategies for enhancing the cycling stability and rate capacity of $LiNi_{0.5}Mn_{1.5}O_4$ as high-voltage cathode materials for high power lithium-ion batteries, J. Power Sources 316 (2016) 85–105.

[68] K. Stokes, T. Kennedy, G. Kim, et al., Influence of carbonate-based additives on the electrochemical performance of Si NW anodes cycled in an ionic liquid electrolyte, Nano Lett. 20 (2020) 7011–7019.

[69] Y. Zhang, Z. Wang, F. Yu, et al., Studies on stability and capacity for long-life cycle performance of $Li(Ni_{0.5}Co_{0.2}Mn_{0.3})O_2$ by Mo modification for lithium-ion battery, J. Power Sources 358 (2017) 1–12.

[70] X. Xiong, D. Ding, Y. Bu, et al., Enhanced electrochemical properties of a LiNiO2-based cathode material by removing lithium residues with $(NH_4)_2HPO_4$, J. Mater. Chem. A 2 (2014) 11691–11696.

[71] I. Anconina, D. Golodnitsky, Electrophoretically deposited artificial cathode electrolyte interphase for improved performance of NMC622 at high voltage operation, RSC Appl. Interfaces 2 (2025) 261–278.

[72] A. Dauth, J. Love, Synthesis and reactivity of 2-azametallacyclobutanes, Dalton Trans. 41 (2012) 7782–7791.

[73] D. Ma, J. Wang, H. Wang, et al., Mg^{2+} and Cr^{3+} co-doped $LiNi_{0.5}Mn_{1.5}O_4$ derived from Ni/Mn bimetal oxide as high-performance cathode for lithium-ion batteries, Nanomaterials 15 (2025) 429.

[74] J. Ma, P. Hu, G. Cui, et al., Surface and interface issues in spinel $LiNi_{0.5}Mn_{1.5}O_4$: insights into a potential cathode material for high energy density lithium ion batteries, Chem. Mater. 28 (2016) 3578–3606.

[75] W. Ou, S.D. Marks, R.F. de Menezes, et al., Unveiling the mechanism of Mn dissolution through a dynamic cathode-electrolyte interphase on $LiMn_2O_4$, Adv. Energy Mater. 15 (2025) 2404652.

[76] L. Rynearson, C. Antolini, C. Jayawardana, et al., Speciation of transition metal dissolution in electrolyte from common cathode materials, Angew. Chem. Int. Ed. Engl. 63 (2024) e202317109.

[77] D. Guan, J. Zeng, Z. Xue, et al., Rational design of the Li^+-solvation structure contributes to constructing a robust cathode-electrolyte interphase for a 5 V high-voltage $LiNi_{0.5}Mn_{1.5}O_4$ cathode, ACS Appl. Energy Mater. 6 (2023) 9568–9576.